UC Santa Barbara

UC Santa Barbara Previously Published Works

Title

Rapid and Tunable Assisted-Microwave Preparation of Glass and Glass-Ceramic Thiophosphate â��Li

7
P

3
S

11
â�� Li-Ion Conductors

Permalink

https://escholarship.org/uc/item/6rm748j2

Journal

ACS Applied Materials & Interfaces, 11(45)

ISSN

1944-8244 1944-8252

Authors

Preefer, Molleigh B
Grebenkemper, Jason H
Schroeder, Franziska
et al.

Publication Date

2019-11-04

DOI

10.1021/acsami.9b15688

Peer reviewed

eScholarship.org Powered by the California Digital Library
University of California

Rapid and Tunable Assisted-Microwave Preparation of Glass and Glass-Ceramic Thiophosphate "$Li_7P_3S_{11}$" Li-ion Conductors

Molleigh B. Preefer,[†,‡] Jason H. Grebenkemper,[‡] Franziska Schroeder,[‡] Joshua D. Bocarsly,[¶,‡] Kartik Pilar,[‡] Joya A. Cooley,[‡] William Zhang,[†] Jerry Hu,[‡] Sumohan Misra,[§] Fabian Seeler,[§] Kerstin Schierle-Arndt,[§] and Ram Seshadri*[,‡,¶,†]

†*Department of Chemistry and Biochemistry, University of California Santa Barbara, California 93106, United States*

‡*Materials Research Laboratory, University of California Santa Barbara, California 93106, United States*

¶*Materials Department, University of California Santa Barbara, California 93106, United States*

§*BASF SE, 67056 Ludwigshafen, Germany*

E-mail: seshadri@mrl.ucsb.edu

Abstract

Glass and glass-ceramic samples of metastable lithium thiophosphates with compositions of $70Li_2S$-$30P_2S_5$ and $Li_7P_3S_{11}$ were controllably prepared using a rapid assisted-microwave procedure in under 30 minutes. The rapid preparation times and weak coupling of the evacuated silica ampoules with microwave radiation ensures minimal reactivity of the reactants and the container. The microwave prepared samples display comparable conductivity values with more conventionally prepared (melt quenched) glass and glass-ceramic samples, on the order of $0.1\,\mathrm{mS\,cm^{-1}}$ and $1\,\mathrm{mS\,cm^{-1}}$ at room temperature, respectively. Rietveld analysis of synchrotron X-ray diffraction data acquired with an internal standard quantitatively yields phase amounts of the glassy and amorphous components, establishing the tunable nature of the microwave preparation. X-ray photoelectron spectroscopy and Raman spectroscopy confirm the composition and the appropriate ratios of isolated and corner-sharing tetrahedra in these semi-crystalline systems. Solid state ^{7}Li nuclear magnetic resonance (NMR) spectroscopy resolve the seven crystallographic Li sites in the crystalline compound into three main environments. The diffusion behavior of these Li environments as obtained from pulsed-field gradient NMR methods can be separated into one slow and one fast component. The rapid and tunable approach to the preparation of high quality "$Li_7P_3S_{11}$" samples presented here, coupled with detailed structural and compositional analysis opens the door to new and promising metastable solid electrolytes.

Keywords

solid electrolyte, lithium-ion conductor, sulfides, glass ceramic, $Li_7P_3S_{11}$

Introduction

All-solid-state batteries are promising candidates to replace some current applications of lithium-ion batteries employing liquid electrolytes, and may potentially enable beyond Li-ion chemistries such as the conversion based Lithium-sulfur system.[1,2] Crucial to enabling all-solid-state batteries is the ability to replace conventional liquid electrolytes with one that is solid, demonstrated to potentially include materials ranging from polymers to ceramic oxides and sulfides.[3,4] Realization of all-solid-state batteries would avoid the hazards of flammable and corrosive liquid electrolytes, simplify construction of the cell by potentially eliminating the need for a separator, and may offer greater stability at higher voltages.[5,6] Beyond improving upon these features of current Li-ion technologies, all-solid-state batteries also open new potential applications in more extreme environments because they can safely operate at higher temperatures, in fact often with improved performance.[7]

The fundamental requirements of a solid electrolyte include having high ionic conductivity (on the order of $1\,mS\,cm^{-1}$ at room temperature), no electronic conductivity, and thermodynamic and kinetic stability versus the anode and cathode materials of choice. Lithium thiophosphates are some of the leading materials to realize all-solid-state batteries, due to their high ionic conductivity. There are many related materials within the family of lithium thiophosphate solid electrolytes, including the thio-LISICONs incorporating Ge,[8–10] Sn,[11] and Si,[12,13] as well as argyrodites and other halogen-containing thiophosphates.[14–17] Within the pure Li–P–S phases, there are three main compositions studied both fundamentally and in battery applications: $Li_7P_3S_{11}$ [Figure 1(a)], Li_3PS_4 [Figure 1(b)], and $Li_4P_2S_6$ [Figure 1(c)], in decreasing order of room temperature conductivities.[18–20] In terms of their structure, Li_3PS_4 and $Li_4P_2S_6$ can be thought of as end-members, where Li_3PS_4 exclu-

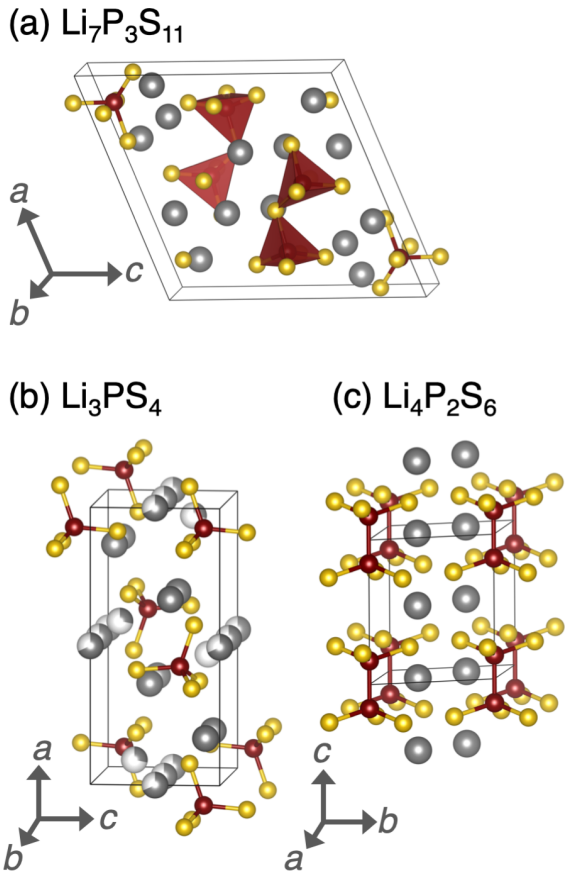

Figure 1: Crystal structures of related lithium thiophosphates (a) $Li_7P_3S_{11}$, (b) Li_3PS_4, and (c) $Li_4P_2S_6$. $Li_7P_3S_{11}$ is the focus of this work, but this series demonstrates the increase in isolated tetrahedra with higher S:P content.

sively has PS_4^{3-} isolated tetrahedra, $Li_4P_2S_6$ exclusively has $P_2S_6^{4-}$ dumbells, and $Li_7P_3S_{11}$ has a mixture of PS_4^{3-} isolated and $P_2S_7^{4-}$ corner-sharing tetrahedra. Of the three phases, $Li_7P_3S_{11}$ is the only metastable phase, and is therefore often observed co-mingled with some percentage of the other two phases, especially $Li_4P_2S_6$.[21] In addition, while the two end-member phases are crystalline, $Li_7P_3S_{11}$ forms as a glass-ceramic phase, which consists of domains of crystalline solid in an amorphous matrix.[22] $Li_7P_3S_{11}$ has been reported to achieve conductivity values on the order of liquid electrolytes such as $LiPF_6$ in ethylene carbonate and dimethyl carbonate, although this is highly dependent on the processing conditions.[23,24] In relation to the last requirement listed, the intrinsic interfacial instability of lithium thiophosphates and lithium is well documented through electrochemical testing in symmetric cells versus lithium, but can be overcome through several engineering routes,

including recent evidence of successfully incorporating surface layers onto the solid electrolyte that are stable to lithium.[24–30] There have been several examples to date of using the $Li_7P_3S_{11}$ solid electrolyte system to date in both Li-ion and Li-S cells.[31–33]

Microwave-based methods provide convenient routes to generating a range of materials and have been successfully employed for preparing chalcogenide and pnictide compounds.[34–37] In a category of materials in which the balance between the degree of crystallinity will be a dictating factor in device performance, a tunable synthesis of this nature is highly desirable.[38] The most common reported synthetic method for the $70\,Li_2S-30\,P_2S_5$ glass has been melt quenching from greater than 700 °C in order to form an amorphous glass, which can then be subsequently annealed between 260 °C and 280 °C to form the glass-ceramic – that is, varying contents of $Li_7P_3S_{11}$ stabilized in the amorphous $70\,Li_2S-30\,P_2S_5$ glass matrix.[39–41] Alternatively, the glass-ceramic can be formed directly through melt quenching from 800 °C.[42] These procedures often result in impurities from the less ionically conductive $Li_4P_2S_6$ phase, however.[43–46] This is because the metastable $Li_7P_3S_{11}$ phase only forms in very narrow temperature regimes, as detailed above. Other syntheses for the glass have involved mechanical milling or solution-phase methods, both requiring further annealing to precipitate crystalline $Li_7P_3S_{11}$ domains.[47–50]

Here we report assisted-microwave preparation wherein the glass can be made in 18 minutes, as well as a direct, one-step preparation of the the glass-ceramic in 28 minutes with extremely low to undetectable amounts of the undesirable, yet highly stable $Li_4P_2S_6$ phase. The highly varied nature of these glass-ceramic materials, comprising significant amorphous and crystalline components, makes a range of techniques essential in order to capture the average structure and crystallinity, as well as local structure information. Therefore, the samples are carefully characterized by a combination of synchrotron X-ray diffraction, X-ray photoelectron spectroscopy, Raman spectroscopy, and solid state ^7Li nuclear magnetic resonance spectroscopy in order to capture the structure-property relationships stemming from the combination of amorphous and crystalline materials.

Methods

Microwave preparation of $70Li_2S$–$30P_2S_5$ glass and $Li_7P_3S_{11}$ glass-ceramic Li_2S and P_2S_5 were ground until homogeneous in a 70:30 molar ratio using an agate mortar and pestle in an Ar filled glovebox with H_2O and $O_2 < 0.1$ ppm. For the glass preparation, the powder was pressed into 250 mg 6 mm pellets, which were sealed in 3 inch long, 3/8 inch diameter fused silica ampoules under 0.25 atm of Ar. Two 275 mg pellets were sealed in 3.5 inch ampoules for the glass-ceramic preparation. Each ampoule was buried in the center of a 250 mL alumina crucible filled with activated charcoal (DARCO 12-20 mesh) held in a cylinder of alumina fiberboard insulation and placed off-center in a 1200 W microwave oven (Panasonic NN-SN651B). This was heated at power 4 (*ie.* 40 % of the total power) for 18 min for the glass and power 4 for 28 min for the glass-ceramic, followed by removing the insulation assembly and sample from the microwave oven and quenching the sample tube in water. The longer heating times for the glass-ceramic allows the material to reach higher temperatures, which is in agreement with previous solid-state methods, in which the glass-ceramic can be formed by melt quenching from higher temperatures than for the glass. The conditions presented above were arrived at after extensive trial-and-error. An immediate noticeable advantage of employing microwaves is that since fused silica is a poor susceptor, and being transparent, absorbs convectional heat poorly, the walls of the container do not get very hot. Consequently, there is little or no reaction between the (corrosive-for-silica) contents and the ampoules, as observed from how clean and transparent the ampoules remain.

X-ray photoelectron spectroscopy X-ray photoelectron spectroscopy (XPS) was carried out on a Kratos Axis Ultra X-ray Photoelectron Spectroscopy system with a monochromatic Al source at 1.4 keV. Samples were prepared in an Ar glovebox using a sample holder with a cover that sealed with an O-ring. The entire sample holder was placed into the first vacuum chamber, and when the vacuum reached approximately 10^{-5} Torr, the cover

was removed and the samples were pumped down to 10^{-8} Torr. Photoelectrons at pass energies of 20 eV and 80 eV for survey and high resolution spectra were detected with a multichannel detector. The spectra were fit by the least-squares method to Voigt functions with Shirley baselines using CasaXPS.

Raman spectroscopy Raman spectroscopic measurements were carried out under inert conditions using a Horiba LabRAM ARAMIS Raman spectrometer equipped with a confocal microscope. Samples were prepared in an Ar-filled glovebox by sealing a glass cover slip over the powder sample on a glass microscope slide. Data was collected with a 633 nm laser, 500,μm hole, 500 μm slit, 1200 cm^{-1} grating, 2 second exposures, and 5 spectra averaged, centered at 450 cm^{-1}. To ensure no decomposition of the sample, a control sample was left in air for a day before measuring. No decomposition peaks were observed in the samples reported herein, the peaks of which have also been detailed in previous studies.[51]

Diffraction analysis of amorphous and crystalline components Laboratory powder X-ray diffraction (XRD) data was collected using a Panalytical Empyrean diffractometer with Cu Kα radiation. Powders were protected from the atmosphere utilizing an air sensitive holder containing a zero background plate and a Kapton film window. High resolution synchrotron diffraction data was collected at room temperature at the Advanced Photon Source at Argonne National Laboratories, beamlines 11-BM-B (for the glass) and 11-ID-B (for the glass-ceramic) using an average wavelength of 0.414581 Å. Samples were loaded into kapton capillaries and sealed with epoxy. They were removed from inert atmosphere minutes prior to measurement. Control experiments were also performed on samples purposefully exposed to air prior to measurement to ensure the integrity of the air-free samples. Rietveld analysis was performed using Topas Academic v6. In order to quantitatively determine the crystallinity of the glass-ceramic phases, additional patterns were collected on samples that had been spiked with known quantities of crystalline Si (on the order of 10 wt.%). Multi-phase Rietveld refinement including all phases was performed on these

patterns including the phases $Li_7P_3S_{11}$, $Li_4P_2S_6$, and Si. Based on the difference between the refined Si wt.% and the known spiked wt.%, the amorphous content of the sample was determined according to the following equations:

$$W_{\mathrm{Li_7S_3S_{11}}} = \frac{W_{\mathrm{Si,known}}}{W'_{\mathrm{Si}}} \times W'_{\mathrm{Li_7S_3S_{11}}} \times 100\,\% \tag{1}$$

$$W_{\mathrm{Li_4S_2S_6}} = \frac{W_{\mathrm{Si,known}}}{W'_{\mathrm{Si}}} \times W'_{\mathrm{Li_4S_2S_6}} \times 100\,\% \tag{2}$$

$$W_{\mathrm{amorphous}} = 100\,\% - W_{\mathrm{Li_7S_3S_{11}}} - W_{\mathrm{Li_4S_2S_6}} - W_{\mathrm{Si,\,known}} \tag{3}$$

Here, $W_{\mathrm{Si,known}}$ is the spiked weight percent of Si in the sample, and W'_{Si} is the apparent weight percent of Si from the Rietveld refinement. $W_{\mathrm{Li_7S_3S_{11}}}$ and $W'_{\mathrm{Li_7S_3S_{11}}}$ are respectively the true and apparent weight percents of crystalline $Li_7S_3P_{11}$, and $W_{\mathrm{Li_4S_2S_6}}$ and $W'_{\mathrm{Li_4S_2S_6}}$ are the true and apparent weight percents of the secondary $Li_4S_2S_6$ phase. $W_{\mathrm{amorphous}}$ is the weight percent of the sample that is not crystalline, which is assumed to come solely from the glassy component of the $Li_7S_3P_{11}$ glass-ceramic. Based on this analysis, the percent crystallinity of the $Li_7S_3S_{11}$ can be determined.

Electrochemical impedance spectroscopy Electrochemical impedance spectroscopy was measured using a VMP3 Bio-logic potentiostat from 1 MHz to 1 Hz with a 200 mV sinus amplitude under inert conditions. The samples were sintered under approximately 180 MPa pressure at 90 °C for 12 h before being subject to variable temperature measurements. Equilibrium was ensured for all of the data reported here by repeating measurements in succession at each temperature until each spectrum aligned before proceeding with the next measurement. To ensure robust fits, data was collected from 20 °C to 90 °C in 5 °C increments using an environmental chamber. Spectra were also collected at 10 °C in order to clearly fit equivalent circuits to each sample, using ZFit in the ECLab software.

The custom cell design used is described in detail in the Supporting Information. A vise and a force gauge (Omega) were used to press pellets *in-situ* and apply and monitor pressure throughout the measurements.

Nuclear magnetic resonance Pulsed-field gradient NMR was conducted on a 300 MHz (7.1 T) Bruker Avance NMR spectrometer with a Bruker diffusion probe capable of 3000 G/cm. A stimulated echo pulse sequence with bipolar gradient pulses was utilized to measure ^{7}Li diffusion coefficients at a resonant frequency of 116.6 MHz. The sample temperature was varied from 25 °C to 80 °C in approximately 10 °C increments, with the sample temperature allowed to equilibrate for 20 min. between subsequent measurements. The pulsed-field gradient strength was set to 16 values between 50 G cm^{-1} and 2800 G cm^{-1} for each measurement. The observed signal attenuation was fit to the Stejskal-Tanner equation to obtain diffusion coefficients. ^{7}Li MAS NMR spectra were acquired on a Bruker AVANCE III Ultrashield Plus 800 MHz (18.8T) NMR spectrometer. These experiments were conducted using a Bruker 2.5 mm HX MAS probe at a spinning speed of 30 kHz. The spectra are referenced to LiCl in H_2O and processed using Bruker TopSpin software. The recycle delay was optimized and found to be 3.2 s for quantitative analysis. Single pulse experiments were used to obtain quantitative spectra and a Hahn echo pulse sequence was used to apply a T_2 filter. Peak fitting was performed using the DMFIT software.[52]

Results and discussion

The microwave prepared glass and glass ceramic samples were characterized by a combination of X-ray photoelectron spectroscopy (XPS), Raman spectroscopy, and X-ray diffraction to understand their local and long-range structures. While XPS is a surface technique and is therefore very sensitive to slight surface oxidation or surface inhomogeneities, the survey scan from 600 eV to 0 eV serves as an approximation for elemental composition in the samples. This range encompasses the characteristic S 2s, S 2p, P 2s, and P 2p energies,

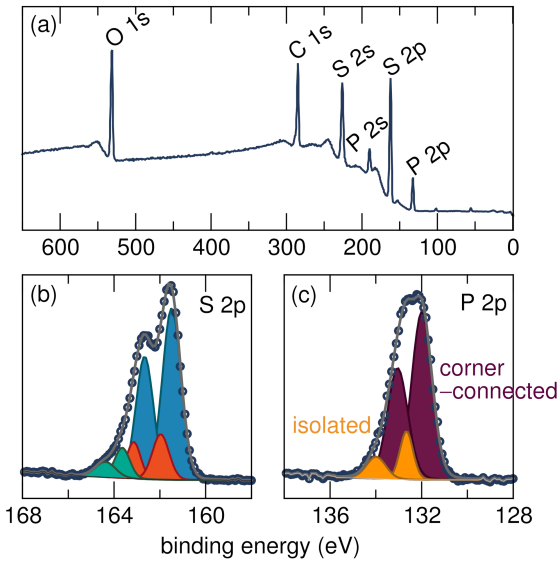

Figure 2: (a) XPS survey region showing elemental composition of a representative glass-ceramic sample. (b) High resolution spectrum in the S binding energy region and (c) high resolution spectrum in the P binding energy region, which shows a higher concentration of the corner sharing tetrahedra as compared to isolated tetrahedra.

allowing quantitative ratios of S:P to be calculated [Figure 2(a)]. The ideal S:P ratio for the targeted $Li_7P_3S_{11}$ stoichiometry is 3.7:1. The glass and glass-ceramic samples synthesized via the one-step microwave preparation range in S:P ratios from 3.8:1 to 4.0:1 between multiple samples for each, which is within reasonable error extrapolating to the bulk material. While the survey scan shows evidence of the O 2p peak, this can be attributed to the stainless steel sample holder and that spectral region does not play in a role in extracting the relative ratios of S:P. High resolution spectra of the S 2p [Figure 2(b)] and P 2p [Figure 2(c)] can be fit to analyze the nature of bonding in these structures. These results are consistent with previous reports and with the known structure of $Li_7P_3S_{11}$ in which there is a higher concentration of the corner-connected tetrahedral environments (seen in the P 2p region) centered at 133 eV to the isolated tetrahedral environments centered at 133.5 eV.[53] The high resolution spectra do not indicate any formation of phosphate species, which would be indicative of oxidation in these samples.

Raman spectroscopy corroborates this local bonding environment picture (Figure 3). The region of the spectrum from 350 cm^{-1} to 450 cm^{-1} includes the modes associated

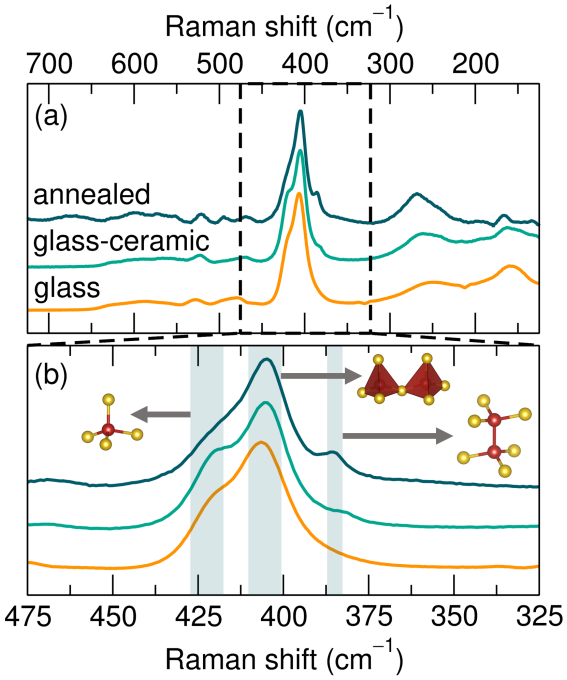

Figure 3: (a) Raman spectra of the glass and glass-ceramic made using assisted-microwave methods, and the subsequently annealed glass-ceramic sample over the full spectral range where peaks are observed. (b) Highlighted spectral region of the modes relating to isolated PS_4^{3-} tetrahedra, corner-sharing tetrahedra (as in $P_2S_7^{4-}$), and $P_2S_6^{4-}$ dumbbells.

with the isolated $PS_4{}^{3-}$ tetrahedra, cotrner-connected $P_2S_7{}^{4-}$ tetrahedral pairs, and $P_2S_6{}^{4-}$ dumbells indicative of $Li_4P_2S_6$ impurity phase when present [Figure 3(b)]. The main modes attributed to the $Li_7P_3S_{11}$ structure are the stretching vibrations of the P-S bonds at 410 cm^{-1} and 425 cm^{-1} for the $P_2S_7{}^{4-}$ and $PS_4{}^{3-}$ anions, respectively. Assignments of these modes are in agreement with several previous reports on $Li_7P_3S_{11}$.[40,54] The glass samples show no signatures of $Li_4P_2S_6$, and the glass-ceramic samples show a hint of the $P_2S_6{}^{4-}$ dumbell centered at 390 cm^{-1}. The presence of the $Li_4P_2S_6$ in the subsequently annealed glass-ceramic is, however, more prominent.

X-ray diffraction yields crucial information about the crystallinity of the microwave-prepared samples, and furnace annealed samples in relation to their conductivities. Crystallization of the $70Li_2S$-$30P_2S_5$ glass into the glass-ceramic is well documented to give superior lithium ionic conductivity, especially when processed in a hot-press setup.[23,40,53,55] However, this is also usually accompanied by some degree of growth of the less-favorable

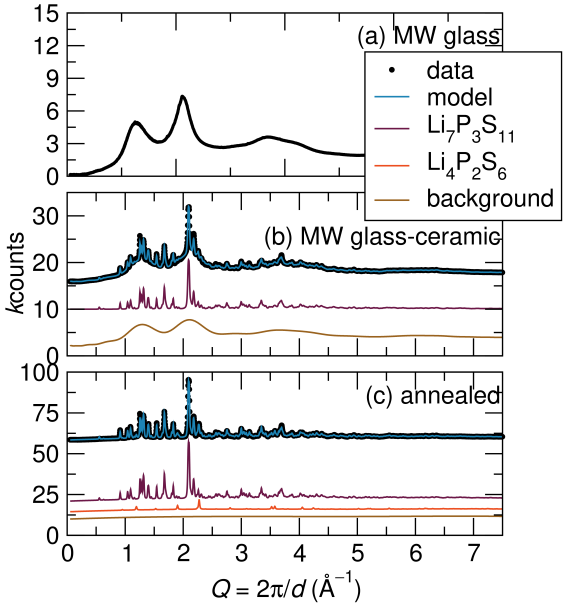

Figure 4: Rietveld refinements from high resolution X-ray diffraction of (a) the microwave-prepared glass, (b) the microwave-prepared glass-ceramic and (c) the microwave-prepared glass-ceramic subsequently annealed at 280 °C for 2 h. The amorphous peaks in the microwave prepared glass and glass-ceramic are due to contributions from the kapton capillary background scattering. The y-axis denotes counts, which can be used to compare the much weaker scattering intensity of the amorphous backgrounds. While the microwave-prepared glass-ceramic sample has a significant amorphous component, the amorphous component significantly decreases in the annealed sample.

$Li_4P_2S_6$ phase.

From laboratory Cu-$K\alpha$ X-ray diffraction, the ability to learn about the glass and glass-ceramic is somewhat limited (Supporting Information Figure S1). In contrast, high-resolution synchrotron X-ray diffraction reveals much more; that a range of states spanning from purely glassy to mostly crystalline is possible. Figure 4(a) shows a high-resolution synchrotron diffraction pattern of the microwaved glass form, showing a complex background with no diffraction peaks, indicating a fully amorphous sample with only short-range order. The microwaved glass-ceramic [Figure 4(b)], on the other hand, shows diffraction peaks for $Li_7P_3S_{11}$ as well as the amorphous background. In part, the diffuse scattering observed is due to the kapton capillary background, and the intensity of the complex amorphous background is much less than the crystalline component evidenced by the counts. Quantitative phase analysis of samples measured with internal Si standards reveal that the $Li_7P_3S_{11}$ is 33(6) % crystalline. The standard deviation on the last significant figure, presented within parentheses, are based upon three identically prepared samples. In these samples, the contribution from $Li_4P_2S_6$ is negligible. Upon further annealing at 280 °C for 2 h, the majority of the amorphous contribution is reduced [Figure 4(c)]. The crystallinity of the $Li_7P_3S_{11}$ increases to 76(3) wt.%, and 8.6(9) wt.% of $Li_4P_2S_6$ grows into the sample. Rietveld refinements for representative samples containing added Si for the quantitative analysis is shown in the Supporting Information (Supporting Information Figure S3), along with a table including the refinement results from several identically-prepared samples.

Since the heating time is much shorter using the microwave preparation and more uniform across the sample, there is less growth of the $Li_4P_2S_6$ phase in contrast to accessing the glass-ceramic by annealing glass in a furnace. The preparation methods employed here also allows for tuning between purely glass and highly crystalline $Li_7P_3S_{11}$ with significant amounts of $Li_4P_2S_6$ impurity. The moderate level of crystallinity from the microwave glass-ceramic synthesis also offers an ideal trade-off between favorable mechanical properties

(more compliant and less grain boundaries) and higher conductivity values than only the pure glass.[38,56]

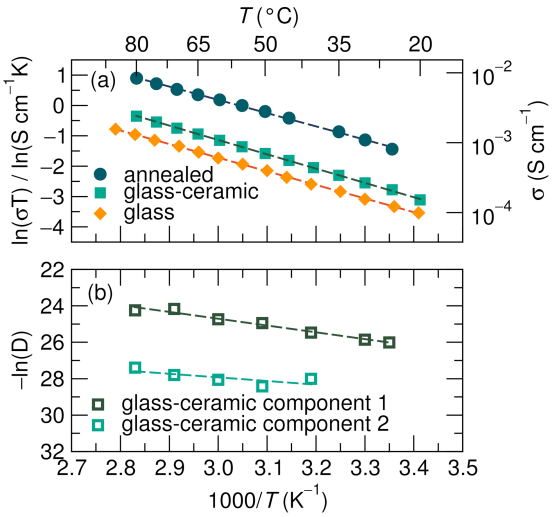

Figure 5: (a) Arrhenius plot of the microwave-prepared glass, glass-ceramic, and subsequently annealed sample, derived from electrochemical impedance spectroscopy at varying temperatures of each sample from 1 MHz to 1 Hz. (b) Arrhenius plot of the two components fit from temperature dependent ^{7}Li pulsed-field gradient NMR of the glass-ceramic, revealing a slower diffusing species and a faster diffusing species within the sample.

The crystalline tuning through the microwave preparation is also reflected in the conductivity values observed through electrochemical impedance spectroscopy in these samples. Arrhenius relationships of the glass, glass-ceramic, and subsequently annealed glass-ceramic align with the percent crystallinity extracted from the Rietveld analyses [Figure 5(a)]. Room temperature conductivity of the microwave-prepared glass is 0.12(1) mS cm^{-1}, while this value is approximately doubled in the microwave-prepared glass ceramic to 0.210(2) mS cm^{-1}. When the glass-ceramic sample is further annealed, the room temperature conductivity increases by an order of magnitude to 1.1 mS cm^{-1}. This is in good agreement with the percent crystallinity doubling from the microwave glass-ceramic to its annealed counterpart.

The activation energies associated with the glass, glass-ceramic, and annealed glass-ceramic can be found through the following Arrhenius-type relationship::[57,58]

$$\sigma T = \sigma_0 \exp\left(\frac{-E_A}{k_B T}\right) \tag{4}$$

where E_A is activation energy, σ_0 is the pre-factor, and k_B is the Boltzmann constant. The Meyer-Neldel compensation rule is applied here due to the intrinsic conductivity of Li in the structure, which has thermally activated hopping (incorporated into the pre-factor term).[59] The activation energies are consistent between the three levels of crystallinity reported here, where the glass is 378(11) meV, the glass-ceramic is 390(15) meV, and the glass-ceramic is 380 meV. The similar activation energies between the annealed glass-ceramic and the one-step microwave prepared glass-ceramic are likely a function of the $Li_4P_2S_6$ present in the annealed glass-ceramic increasing the activation energy in what otherwise should have a lower barrier to diffusion considering the high percentage of overall crystallinity in the samples.

The pulsed-field gradient ^{7}Li NMR of the glass-ceramic indicates that there are two different diffusion processes, one in which Li diffuses slower than the other by approximately an order of magnitude [Figure 5(b)]. This is consistent with previous studies using time-of-flight neutron diffraction to distinguish two lithium conduction pathways and previous temperature-dependent $^{6/7}$Li studies.[60,61] At 40 °C, the first diffusion constant is 8.7×10^{-12} m^2 s^{-1}, while the second component has a diffusion constant of 6.8×10^{-12} m^2 s^{-1}. The overall values are consistent with the electrochemical impedance spectroscopy, as the activation energy of the first component is 320(25) meV, and the activation energy of the second component is 330(22) meV.

By filtering chemical shift environments by T_2 relaxation delays, groupings of Li assignments can be determined experimentally, rather than purely by fitting the peaks to Gaussian curves [Figure 6(a)]. Despite spinning at 30 kHz using an 800 MHz spectrometer, the narrow range of ^{7}Li chemical shifts and line-broadening means the resolution is not sufficient to parse all 7 crystallographic sites. Even with the T_2 filter, only 3 general environments are observed experimentally [Figure 6(b)]. This suggests that the bonding

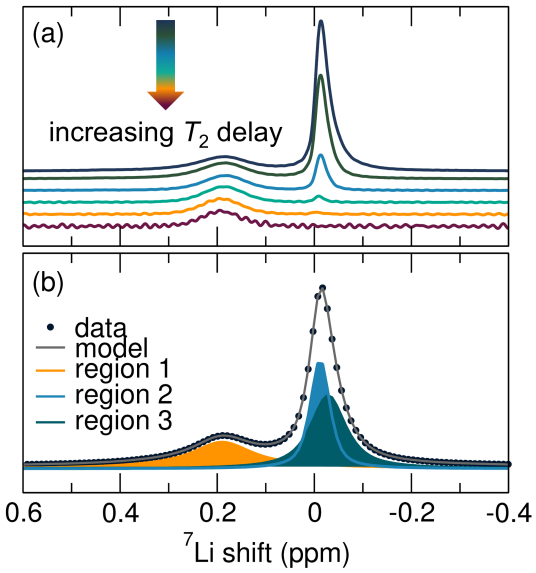

Figure 6: (a) ^{7}Li MAS NMR with varying T_2 delays filters chemical shift environments with similar ion mobilities, indicating the presence of three environments containing similarly behaving lithium sites. (b) ^{7}Li MAS NMR fit with the three discernible regions from the T_2 filter. While we know there are 7 crystallographic sites, they can generally be grouped into these 3 regions.

environments in the structure are not vastly different from each other. Increasing T_2 is indicative of faster motion in these systems (and can be thought of as inversely proportional to line width). The most upfield peak at 0.2 ppm has the longest T_2 delay, though is obviously the broadest peak fit to the spectrum. This indicates that there are multiple Li sites encompassed within this larger peak, likely with sharper line widths, that are indistinguishable from each other in terms of their motion and only very slightly in how shielded they are. The two downfield peaks centered at -0.01 ppm and -0.04 ppm disappear as the T_2 delay increases. Though not certain, it is possible these two peaks correspond to the slower diffusing species identified from the PFG NMR, and the 0.2 ppm general environment corresponds to the faster diffusing species.

Conclusion

Microwave-based preparation methods provide a convenient route to preparing lithium thiophosphate solid electrolytes, especially in light of the inherent thermodynamic metastability of these materials. The synthesis can be tuned to achieve varied levels of crystallinity, and when paired with further annealing, opens a wide range of degree of crystallinity that lends flexibility and tunability of mechanical and ionic transport properties. As discussed in previous literature, this is highly consequential when considering building full cells, where the optimal balance of these properties is paramount. Furthermore, this work highlights the need for rigorous characterization using a multitude of techniques that yield insight into both the crystalline and amorphous components of solid electrolyte materials to fully understand the structure-composition-function-performance relationships in these materials.

Supporting Information Available

Table of quantified crystallinities from Rietveld refinements for identically-prepared glass-ceramic and annealed glass-ceramic samples. Laboratory XRD on three identically prepared samples of the glass-ceramic. Laboratory XRD comparing the glass, glass-ceramic, and annealed glass-ceramic. Rietveld refinements of glass-ceramic and annealed glass-ceramic with Si added from synchrotron data, as well as glass data with added Si. Setup to measure electrochemical impedance spectroscopy under pressure and heat described in detail. Representative electrochemical impedance spectroscopy equivalent circuit fit used to calculate ionic conductivity values. Representative double exponential fit to pulsed field gradient (PFG) NMR data used to calculate diffusion constants. This material is available free of charge via the Internet at `http://pubs.acs.org/`.

Acknowledgement

This work was supported by BASF Corporation through the California Research Alliance. M.B.P. acknowledges support from the Mellichamp Academic Initiative in Sustainability. J.D.B. is supported by the National Science Foundation Graduate Research Fellowship Program under NSF 1650114. The research reported here made use of shared facilities of the UC Santa Barbara Materials Research Science and Engineering Center (MRSEC, NSF DMR 1720256), a member of the Materials Research Facilities Network (www.mrfn.org). Diffraction data was collected at the X-ray Science Division beamlines 11-BM and 11-ID-B at the Advanced Photon Source, Argonne National Laboratory, a U.S. Department of Energy (DOE) Office of Science User Facility operated for the DOE Office of Science by Argonne National Laboratory under Contract No. DE-AC02-06CH11357. We gratefully acknowledge help from Principal Beamline Specialist Kevin Beyer. MBP thanks Douglas Fabini for helpful discussions regarding impedance spectroscopy.

References

(1) Zeier, W.; Janek, J. A Solid Future for Battery Development. *Nat. Energy* **2016**, *1*, 16141.

(2) Zhang, Z.; Shao, Y.; Lotsch, B.; Hu, Y. S.; Li, H.; Janek, J.; Nazar, L. F.; Nan, C. W.; Maier, J.; Armand, M.; Chen, L. New Horizons for Inorganic Solid State Ion Conductors. *Energy Environ. Sci.* **2018**, *11*, 1945–1976.

(3) Goodenough, J. B.; Singh, P. Review–Solid Electrolytes in Rechargeable Electrochemical Cells. *J. Electrochem. Soc.* **2015**, *162*, A2387–A2392.

(4) Manthiram, A.; Yu, X.; Wang, S. Lithium Battery Chemistries Enabled by Solid-State Electrolytes. *Nature Reviews Materials* **2017**, *2*, 16103.

(5) Zhu, Y.; He, X.; Mo, Y. Origin of Outstanding Stability in the Lithium Solid Electrolyte Materials: Insights from Thermodynamic Analyses Based on First-Principles Calculations. *ACS Appl. Mater. Interfaces* **2015**, *7*, 23685–23693.

(6) Kato, Y.; Hori, S.; Saito, T.; Suzuki, K.; Hirayama, M.; Mitsui, A.; Yonemura, M.; Iba, H.; Kanno, R. High-Power All-Solid-State Batteries Using Sulfide Superionic Conductors. *Nat. Energy* **2016**, *1*, 1–7.

(7) Robertson, A.; West, A.; Ritchie, A. Review of Crystalline Lithium-Ion Conductors Suitable for High Temperature Battery Applications. *Solid State Ionics* **1997**, *104*, 1–11.

(8) Kanno, R.; Murayama, M. Lithium Ionic Conductor Thio-LISICON: The Li_2S-GeS_2-P_2S_5 System. *J. Electrochem. Soc.* **2001**, *148*, 742–746.

(9) Kuhn, A.; Duppel, V.; Lotsch, B. V. Tetragonal $Li_{10}GeP_2S_{12}$ and Li_7GePS_8 – Exploring the Li Ion Dynamics in LGPS Li Electrolytes. *Energy Environ. Sci.* **2013**, *6*, 3548–3552.

(10) Weber, D. A.; Senyshyn, A.; Weldert, K. S.; Wenzel, S.; Zhang, W.; Kaiser, R.; Bere,; Ndts, S.; Janek, J.; Zeier, W. G. Structural Insights and 3D Diffusion Pathways within the Lithium Superionic Conductor $Li_{10}GeP_2S_{12}$. *Chem. Mater.* **2016**, *28*, 5905–5915.

(11) Bron, P.; Johansson, S.; Zick, K.; Der Günne, J. S. A.; Dehnen, S.; Roling, B. $Li_{10}SnP_2S_{12}$: An Affordable Lithium Superionic Conductor. *J. Am. Chem. Soc.* **2013**, *135*, 15694–15697.

(12) Kuhn, A.; Gerbig, O.; Zhu, C.; Falkenberg, F.; Maier, J.; Lotsch, B. V. A New Ultrafast Superionic Li-Conductor: Ion Dynamics in $Li_{11}Si_2PS_{12}$ and Comparison with Other Tetragonal LGPS-type Electrolytes. *Phys. Chem. Chem. Phys.* **2014**, *16*, 14669–14674.

(13) Harm, S.; Hatz, A.-K.; Moudrakovski, I.; Eger, R.; Kuhn, A.; Hoch, C.; Lotsch, B. V. Lesson Learned from NMR: Characterization and Ionic Conductivity of LGPS-like Li_7SiPS_8. *Chem. Mater.* **2019**, *31*, 1280–1288.

(14) Rangasamy, E.; Liu, Z.; Gobet, M.; Pilar, K.; Sahu, G.; Zhou, W.; Wu, H.; Greenbaum, S.; Liang, C. An Iodide-Based $Li_7P_2S_8I$ Superionic Conductor. *J. Am. Chem. Soc.* **2015**, *137*, 1384–1387.

(15) De Klerk, N. J.; Rosłoń, I.; Wagemaker, M. Diffusion Mechanism of Li Argyrodite Solid Electrolytes for Li-Ion Batteries and Prediction of Optimized Halogen Doping: The Effect of Li Vacancies, Halogens, and Halogen Disorder. *Chem. Mater.* **2016**, *28*, 7955–7963.

(16) Yu, C.; Ganapathy, S.; Hageman, J.; Van Eijck, L.; Van Eck, E. R.; Zhang, L.; Schwietert, T.; Basak, S.; Kelder, E. M.; Wagemaker, M. Facile Synthesis toward the Optimal Structure-Conductivity Characteristics of the Argyrodite Li_6PS_5Cl Solid-State Electrolyte. *ACS Appl. Mater. Interfaces* **2018**, *10*, 33296–33306.

(17) Adeli, P.; Bazak, J. D.; Park, K. H.; Kochetkov, I.; Huq, A.; Goward, G. R.; Nazar, L. F.

Boosting Solid-State Diffusivity and Conductivity in Lithium Superionic Argyrodites by Halide Substitution. *Angew. Chemie - Int. Ed.* **2019**, *58*, 8681–8686.

(18) Onodera, Y.; Mori, K.; Otomo, T.; Hannon, A. C.; Kohara, S. Crystal Structure of $Li_7P_3S_{11}$ Studied by Neutron and Synchrotron X-ray Powder Diffraction. *J. Phys. Soc. Jpn.* **2010**, *79*, 87–89.

(19) Dietrich, C.; Sadowski, M.; Sicolo, S.; Weber, D. A.; Sedlmaier, S. J.; Weldert, K. S.; Indris, S.; Albe, K.; Janek, J.; Zeier, W. G. Local Structural Investigations, Defect Formation, and Ionic Conductivity of the Lithium Ionic Conductor $Li_4P_2S_6$. *Chem. Mater.* **2016**, *28*, 8764–8773.

(20) Dietrich, C.; Weber, D. A.; Culver, S.; Senyshyn, A.; Sedlmaier, S. J.; Indris, S.; Janek, J.; Zeier, W. G. Synthesis, Structural Characterization, and Lithium Ion Conductivity of the Lithium Thiophosphate $Li_2P_2S_6$. *Inorg. Chem.* **2017**, *56*, 6681–6687.

(21) Yamane, H.; Shibata, M.; Shimane, Y.; Junke, T.; Seino, Y.; Adams, S.; Minami, K.; Hayashi, A.; Tatsumisago, M. Crystal Structure of a Superionic Conductor, $Li_7P_3S_{11}$. *Solid State Ionics* **2007**, *178*, 1163–1167.

(22) Mizuno, F.; Hayashi, A.; Tadanaga, K.; Tatsumisago, M. New, Highly Ion-Conductive Crystals Precipitated from Li_2S-P_2S_5 Glasses. *Adv. Mater.* **2005**, *17*, 918–921.

(23) Seino, Y.; Ota, T.; Takada, K.; Hayashi, A.; Tatsumisago, M. A Sulphide Lithium Super Ion Conductor is Superior to Liquid Ion Conductors for Use in Rechargeable Batteries. *Energy Environ. Sci.* **2014**, *7*, 627–631.

(24) Chu, I.-h. H.; Nguyen, H.; Hy, S.; Lin, Y.-c. C.; Wang, Z.; Xu, Z.; Deng, Z.; Meng, Y. S.; Ong, S. P. Insights into the Performance Limits of the $Li_7P_3S_{11}$ Superionic Conductor: A Combined First-Principles and Experimental Study. *ACS Appl. Mater. Interfaces* **2016**, *8*, 7843–7853.

(25) Berbano, S. S.; Mirsaneh, M.; Lanagan, M. T.; Randall, C. A. Lithium Thiophosphate Glasses and Glass-Ceramics as Solid Electrolytes: Processing, Microstructure, and Properties. *Int. J. App. Glass Sci.* **2013**, *4*, 414–425.

(26) Richards, W. D.; Miara, L. J.; Wang, Y.; Kim, J. C.; Ceder, G. Interface Stability in Solid-State Batteries. *Chem. Mater.* **2016**, *28*, 266–273.

(27) Wenzel, S.; Weber, D. A.; Leichtweiss, T.; Busche, M. R.; Sann, J.; Janek, J. Interphase Formation and Degradation of Charge Transfer Kinetics Between a Lithium Metal Anode and Highly Crystalline $Li_7P_3S_{11}$ Solid Electrolyte. *Solid State Ionics* **2016**, *286*, 24–33.

(28) Kerman, K.; Luntz, A.; Viswanathan, V.; Chiang, Y.-m.; Chen, Z. Review Practical Challenges Hindering the Development of Solid State Li Ion Batteries. *J. Electrochem. Soc.* **2017**, *164*, 1731–1744.

(29) Culver, S. P.; Koerver, R.; Krauskopf, T.; Zeier, W. G. Designing Ionic Conductors: The Interplay between Structural Phenomena and Interfaces in Thiophosphate-Based Solid-State Batteries. *Chem. Mater.* **2018**, *30*, 4179–4192.

(30) Xu, R.; Han, F.; Ji, X.; Fan, X.; Tu, J.; Wang, C. Interface Engineering of Sulfide Electrolytes for All-Solid-State Lithium Batteries. *Nano Energy* **2018**, *53*, 958–966.

(31) Minami, T.; Hayashi, A.; Tatsumisago, M. Recent Progress of Glass and Glass-Ceramics as Solid Electrolytes for Lithium Secondary Batteries. *Solid State Ionics* **2006**, *177*, 2715–2720.

(32) Yamada, T.; Ito, S.; Omoda, R.; Watanabe, T.; Aihara, Y.; Agostini, M.; Ulissi, U.; Hassoun, J.; Scrosati, B. All Solid-State Lithium-Sulfur Battery Using a Glass-Type P_2S_5-Li_2S Electrolyte: Benefits on Anode Kinetics. *J. Electrochem. Soc.* **2015**, *162*, A646–A651.

(33) Yao, X.; Liu, D.; Wang, C.; Long, P.; Peng, G.; Hu, Y. S.; Li, H.; Chen, L.; Xu, X. High-Energy All-Solid-State Lithium Batteries with Ultralong Cycle Life. *Nano Lett.* **2016**, *16*, 7148–7154.

(34) Grebenkemper, J. H.; Bocarsly, J. D.; Levin, E. E.; Seward, G.; Heikes, C.; Brown, C.; Misra, S.; Seeler, F.; Schierle-Arndt, K.; Wilson, S. D.; Seshadri, R. Rapid Microwave Preparation and Composition Tuning of the High-Performance Magnetocalorics $(Mn,Fe)_2(P,Si)$. *ACS Appl. Mater. Interfaces* **2018**, *10*, 7208–7213.

(35) Butala, M. M.; Perez, M. A.; Arnon, S.; Göbel, C.; Preefer, M. B.; Seshadri, R. Rapid Microwave-Assisted Preparation of Binary and Ternary Transition Metal Sulfide Compounds. *Solid State Sci.* **2017**, *74*, 8–12.

(36) Mastrovito, C.; Lekse, J. W.; Aitken, J. A. Rapid Solid-State Synthesis of Binary Group 15 Chalcogenides using Microwave Irradiation. *J. Solid State Chem.* **2007**, *180*, 3262–3270.

(37) Levin, E. E.; Grebenkemper, J. H.; Pollock, T. M.; Seshadri, R. Protocols for High Temperature Assisted-Microwave Preparation of Inorganic Compounds. *Chem. Mater.* **2019**, *31*, 7151–7159.

(38) McGrogan, F. P.; Swamy, T.; Bishop, S. R.; Eggleton, E.; Porz, L.; Chen, X.; Chiang, Y. M.; Van Vliet, K. J. Compliant Yet Brittle Mechanical Behavior of Li_2S-P_2S_5 Lithium-Ion-Conducting Solid Electrolyte. *Adv. Energy Mater.* **2017**, *7*, 1–5.

(39) Minami, K.; Hayashi, A.; Tatsumisago, M. Crystallization Process for Superionic $Li_7P_3S_{11}$ Glass-Ceramic Electrolytes. *J. Am. Ceram. Soc.* **2011**, *94*, 1779–1783.

(40) Mizuno, F.; Hayashi, A.; Tadanaga, K.; Tatsumisago, M. New Lithium-Ion Conducting Crystal Obtained by Crystallization of the Li_2S-P_2S_5 glasses. *Electrochemical and Solid-State Letters* **2005**, *8*, 603–606.

(41) Kudu, Ö. U.; Famprikis, T.; Fleutot, B.; Braida, M. D.; Le Mercier, T.; Islam, M. S.; Masquelier, C. A Review of Structural Properties and Synthesis Methods of Solid Electrolyte Materials in the $Li_2SP_2S_5$ Binary System. *Journal of Power Sources* **2018**, *407*, 31–43.

(42) Minami, K.; Hayashi, A.; Tatsumisago, M. Preparation and Characterization of Superionic Conducting $Li_7P_3S_{11}$ Crystal from Glassy Liquids. *J. Ceram. Soc. Japan* **2010**, *118*, 305–308.

(43) Hayashi, A.; Shigenori, H.; Mizuno, F.; Tadanaga, K.; Minami, T.; Tatsumisago, M. Characterization of Li_2S-P_2S_5 Glass-Ceramics as a Solid Electrolyte for Lithium Secondary Batteries. *Solid State Ionics* **2004**, *175*, 683–686.

(44) Hayashi, A.; Minami, K.; Mizuno, F.; Tatsumisago, M. Formation of Li^+ Superionic Crystals from the Li_2S-P_2S_5 Melt-Quenched Glasses. *J. Mater. Sci.* **2008**, *43*, 1885–1889.

(45) Hayashi, A.; Minami, K.; Tatsumisago, M. Development of Sulfide Glass-Ceramic Electrolytes for All-Solid-State Lithium Rechargeable Batteries. *J. Solid State Electrochem.* **2010**, *14*, 1761–1767.

(46) Seino, Y.; Nakagawa, M.; Senga, M.; Higuchi, H.; Takada, K.; Sasaki, T. Analysis of the Structure and Degree of Crystallisation of $70Li_2S$-$30P_2S_5$ Glass Ceramic. *J. Mater. Chem. A* **2015**, *3*, 2756–2761.

(47) Hayashi, A.; Shigenori, H.; Morimoto, H.; Tatsumisago, M.; Minami, T. Preparation of Li_2S-P_2S_5 Amorphous Solid Electrolytes by Mechanical Milling. *J. Am. Ceram. Soc.* **2001**, *84*, 477–479.

(48) Xu, R. C.; Xia, X. H.; Yao, Z. J.; Wang, X. L.; Gu, C. D.; Tu, J. P. Preparation of $Li_7P_3S_{11}$ Glass-Ceramic Electrolyte by Dissolution-Evaporation Method for All-Solid-State Lithium Ion Batteries. *Electrochim. Acta* **2016**, *219*, 235–240.

(49) Xue, B.; Fan, B.; Li, B.; Chen, L.; Wang, F.; Luo, Z.; Zhang, X.; Ma, H. Solvent-Assisted Ball Milling for Synthesizing Solid Electrolyte $Li_7P_3S_{11}$. *J. Am. Ceram. Soc.* **2019**, *102*, 3402–3410.

(50) Wang, Y.; Lu, D.; Bowden, M.; Khoury, P. Z. E.; Han, K. S.; Deng, Z. D.; Xiao, J.; Zhang, J.-g.; Liu, J. Mechanism of Formation of $Li_7P_3S_{11}$ Solid Electrolytes through Liquid Phase Synthesis. *Chem. Mater.* **2018**, *30*, 990–997.

(51) Muramatsu, H.; Hayashi, A.; Ohtomo, T.; Hama, S.; Tatsumisago, M. Structural Change of Li_2S-P_2S_5 Sulfide Solid Electrolytes in the Atmosphere. *Solid State Ionics* **2011**, *182*, 116–119.

(52) Massiot, D.; Fayon, F.; Capron, M.; King, I.; Le Calve, S.; Alonso, B.; Durand, J.-O.; Bujoli, B.; Zhehong, G.; Hoatson, G. Modelling One- and Two-Dimensional Solid-State NMR Spectra. *Magnetic Resonance in Chemistry* **2002**, *40*, 70–76.

(53) Busche, M. R.; Weber, D. A.; Schneider, Y.; Dietrich, C.; Wenzel, S.; Leichtweiss, T.; Schröder, D.; Zhang, W.; Weigand, H.; Walter, D.; Sedlmaier, S. J.; Houtarde, D.; Nazar, L. F.; Janek, J. In Situ Monitoring of Fast Li-Ion Conductor $Li_7P_3S_{11}$ Crystallization Inside a Hot-Press Setup. *Chem. Mater.* **2016**, *28*, 6152–6165.

(54) Mizuno, F.; Hayashi, A.; Tadanaga, K.; Tatsumisago, M. High Lithium Ion Conducting Glass-Ceramics in the System Li_2S-P_2S_5. *Solid State Ionics* **2006**, *177*, 2721–2725.

(55) Garcia-Mendez, R.; Mizuno, F.; Zhang, R.; Arthur, T. S.; Sakamoto, J. Effect of Processing Conditions of $75Li_2S$-$25P_2S_5$ Solid Electrolyte on its DC Electrochemical Behavior. *Electrochim. Acta* **2017**, *237*, 144–151.

(56) Lau, J.; DeBlock, R. H.; Butts, D. M.; Ashby, D. S.; Choi, C. S.; Dunn, B. S. Sulfide Solid Electrolytes for Lithium Battery Applications. *Adv. Energy Mater.* **2018**, *8*, 1–24.

(57) Meyer, W.; Neldel, H. Relation Between the Energy Constant and the Quantity Constant in the Conductivity–Temperature Formula of Oxide Semiconductors. *Z. Tech. Phys* **1937**, *18*, 588–593.

(58) Tilley, R. J. *Defects in Solids*; John Wiley & Sons, 2008; Vol. 4.

(59) Yelon, A.; Movaghar, B. The Meyer-Neldel Conductivity Prefactor for Chalcogenide Glasses. *Appl. Phys. Lett.* **1997**, *71*, 3549–3551.

(60) Mori, K.; Ichida, T.; Iwase, K.; Otomo, T.; Kohara, S.; Arai, H.; Uchimoto, Y.; Ogumi, Z.; Onodera, Y.; Fukunaga, T. Visualization of Conduction Pathways in Lithium Superionic Conductors: Li_2S-P_2S_5 Glasses and $Li_7P_3S_{11}$ GlassCeramic. *Chem. Phys. Lett.* **2013**, *584*, 113–118.

(61) Murakami, M.; Shimoda, K.; Shiotani, S.; Mitsui, A.; Ohara, K.; Onodera, Y.; Arai, H.; Uchimoto, Y.; Ogumi, Z. Dynamical Origin of Ionic Conductivity for $Li_7P_3S_{11}$ Metastable Crystal As Studied by $^{6/7}$Li and ^{31}P Solid-State NMR. *J. Phys. Chem. C* **2015**, *119*, 24248–24254.

Graphical TOC Entry

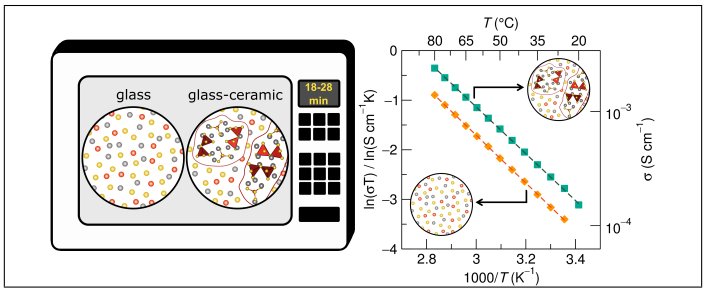

Supporting Information: Rapid and Tunable Assisted-Microwave Preparation of Glass and Glass-Ceramic Thiophosphate "$Li_7P_3S_{11}$" Li-ion Conductors

Molleigh B. Preefer,[†,‡] Jason H. Grebenkemper,[‡] Franziska Schroeder,[‡] Joshua D. Bocarsly,[¶,‡] Kartik Pilar,[‡] Joya A. Cooley,[‡] William Zhang,[†] Jerry Hu,[‡] Sumohan Misra,[§] Fabian Seeler,[§] Kerstin Schierle-Arndt,[§] and Ram Seshadri[*,‡,¶,†]

†*Department of Chemistry and Biochemistry, University of California Santa Barbara, California 93106, United States*

‡*Materials Research Laboratory, University of California Santa Barbara, California 93106, United States*

¶*Materials Department, University of California Santa Barbara, California 93106, United States*

§*BASF SE, 67056 Ludwigshafen, Germany*

E-mail: seshadri@mrl.ucsb.edu

sample	$Li_4P_2S_6$ wt.-%	$Li_7P_3S_{11}$ % crystallinity	a (Å)	b (Å)	c (Å)	α (°)	β (°)	γ (°)	V (Å^3)
	MW glass ceramic								
1	0	25.6(4)	12.540(2)	6.0289(9)	12.531(2)	102.53(2)	113.42(2)	74.33(2)	830.6(3)
2	1.6(1)	22.9(3)	12.533(2)	6.0285(8)	12.527(2)	102.53(2)	113.38(1)	74.34(2)	830.0(2)
3	2.8(1)	35.5(3)	12.545(1)	6.0285(5)	12.532(1)	102.59(1)	113.456(9)	74.29(1)	830.4(2)
4[a]	0	33.0(5)	12.522(2)	6.0264(7)	12.530(1)	102.58(1)	113.32(1)	74.44(1)	829.8(2)
5[a]	0	40.7(5)	12.548(1)	6.0285(5)	12.528(1)	102.61(1)	113.358(9)	74.38(1)	831.2(2)
	MW glass ceramic + 2 hr anneal								
1[b]	5.4*		12.538(1)	6.0279(4)	12.5282(8)	102.666(7)	113.377(6)	74.385(8)	830.2(1)
2	8.6(2)	76(1)	12.529(1)	6.0271(5)	12.528(1)	102.626(10)	113.419(8)	74.360(10)	829.3(1)
3	10.5(2)	82(1)	12.533(1)	6.0261(5)	12.5272(9)	102.615(8)	113.419(7)	74.350(8)	829.4(1)

[a] Samples 4 and 5 were not annealed. [b] Sample 1 was not measured with a Si standard after annealing, so percent crystallinity is not available. The weight percent of $Li_4P_2S_6$ is estimated from Rietveld of the standard-less diffraction data by assuming the $Li_7P_3S_{11}$ % phase is 79% crystalline.

Table 1: Phase fractions and lattice parameters from Rietveld refinements of replicate samples of the glass (top) and glass-ceramic (bottom). These samples were used to calculate the standard deviations of the crystallinity percentages discussed in the main text.

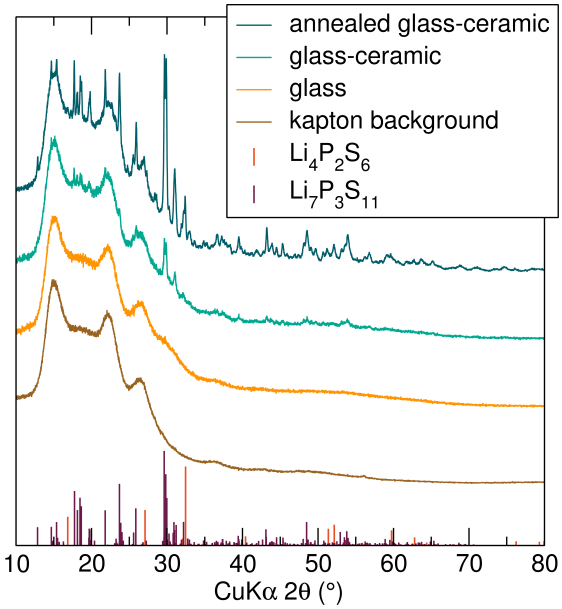

Figure S1: X-ray diffraction of the glass, glass-ceramic, and annealed glass-ceramic from a laboratory Cu $k\alpha$ radiation source in a kapton holder to maintain an air-free environment. The kapton background obscures the true nature of the background, but there is a clear progression from more amorphous (glass) to more crystalline (annealed glass-ceramic). However, to fully understand how crystalline the sample is, a key property relating to the conductivity in these samples, high energy X-ray diffraction must be used.

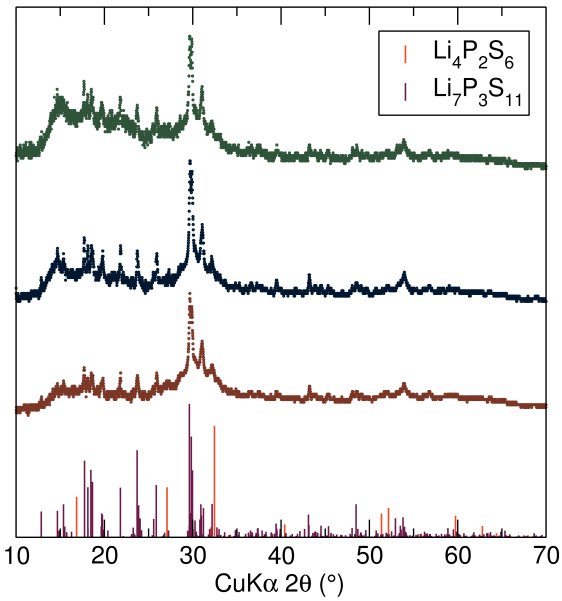

Figure S2: XRD patterns of three identically prepared glass-ceramic samples show similar patterns matching the reflections of $Li_7P_3S_{11}$ from the laboratory Cu $k\alpha$ radiation source.

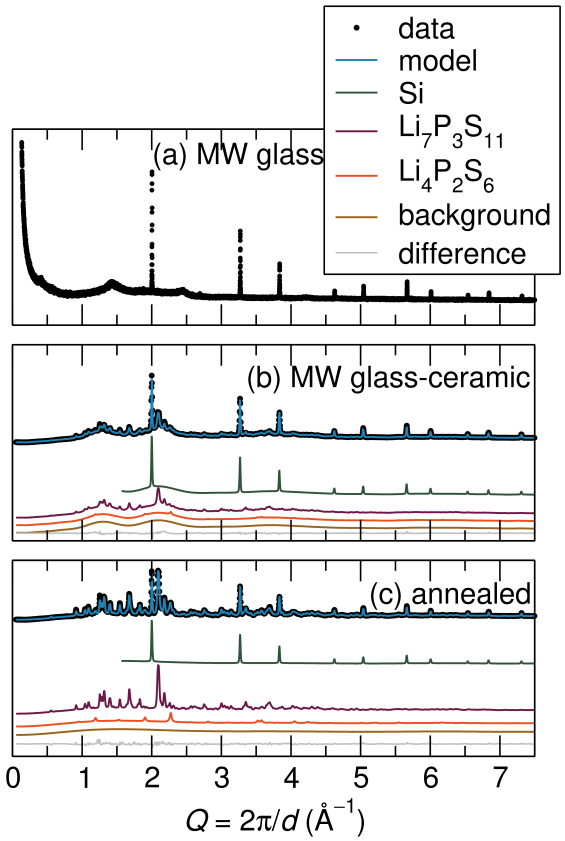

Figure S3: Synchrotron X-ray diffraction on (a) a microwave glass sample (from APS 11-BM at Argonne National Lab), (b) microwave glass-ceramic sample (from APS 11-ID-B at Argonne National Lab), and (c) annealed microwave glass-ceramic sample (from APS 11-ID-B at Argonne National Lab) with Si added for crystallinity analyses. The glass does not show any discernible crystalline peaks, so no crystallinity analysis was performed. The microwave glass-ceramic shows negligible $Li_4P_2S_6$ present in the sample ($<2\,\%$), while in the annealed sample the $Li_4P_2S_6$ grows to a significant proportion of the model.

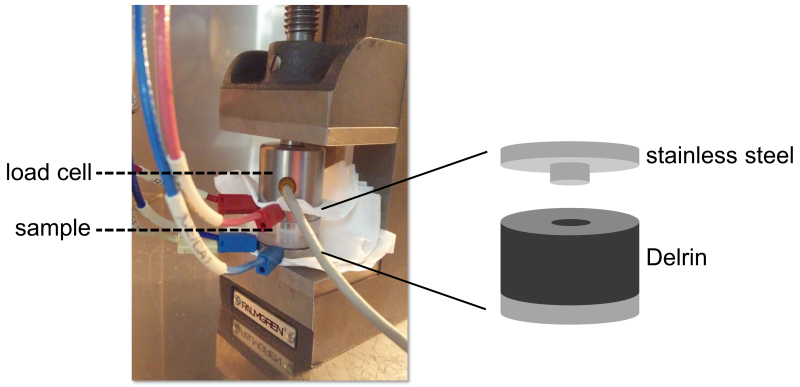

Figure S4: The photograph on the left shows the impedance cell, load cell, and vise used to apply pressure on the sample while keeping it air-free for the duration of temperature-dependent measurements. The entire apparatus was inserted into a temperature chamber and allowed to equilibrate fully between measurements to ensure steady-state processes were probed. The body of the cell is constructed from Delrin, and the end-caps were machined from 316 stainless steel to have a tight slip with the body (6 mm cavity). The samples were loaded in an Ar glovebox, and the end-caps were greased with vacuum grease. Once placed in the antechambers, the antechambers were evacuated to create a good seal between the end-caps and the body of the cell before being removed. Either kimwipes or sheets of acrylic were used to insulate the cell from the load cell and vise. The cells were allowed to sinter overnight at the highest temperature of measurement at 5 kN. The force would relax to roughly 4 kN. Before measurement, the vise was retightened to 5 kN and stayed stable at this force throughout the measurement.

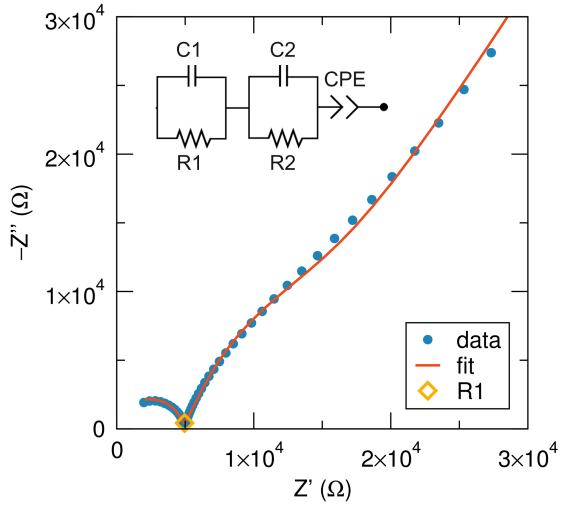

Figure S5: A representative Nyquist plot showing the equivalent circuit fit applied to all of the spectra. This single circuit fit all of the spectra from sample to sample as well as at different temperatures. The R1 value can be attributed to the defined semicircle, which is indicative of the ionic conductivity of the Li within the sample.)

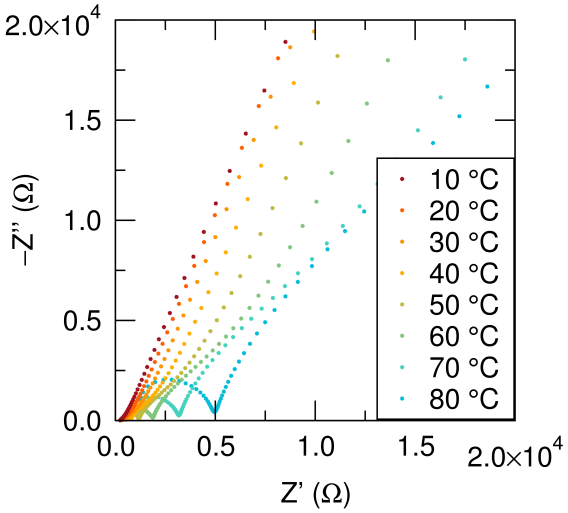

Figure S6: Nyquist plots presenting the temperature dependent data for the glass-ceramic (similar spectra were acquired for the glass and annealed glass-ceramic samples) from 10 °C to 80 °C. By fitting these spectra to the above equivalent circuit and extracting the resistance of the defined semicircle, we were able to calculate ionic conductivity values as a function of temperature, leading to the Arrhenius plots presented in the main text.)

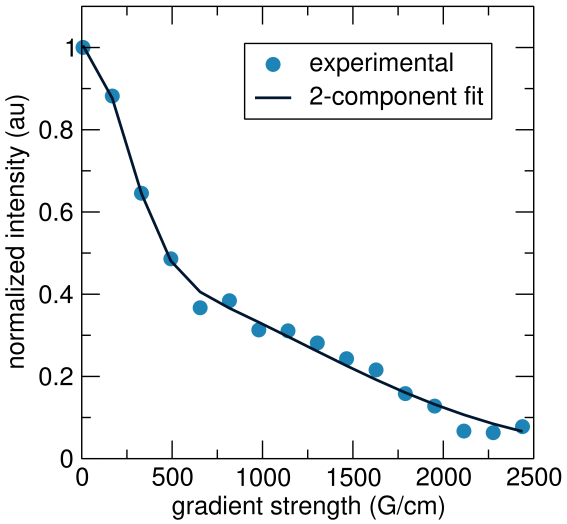

Figure S7: ^{7}Li pulsed field diffusion NMR double exponential fit of the intensity as a function of the gradient field strength. The need for a double exponential fit arises from two different diffusion processes occurring at different time scales.